

A Decade of QuikSCAT Scatterometer Sea Ice Extent Data

Quinn P. Remund, *Member, IEEE*, and David G. Long, *Fellow, IEEE*

Abstract—Polar sea ice is an important input to global climate models and is considered to be a sensitive indicator of climate change. While originally designed only for wind estimation, radar backscatter measurements collected by wind scatterometers have proven useful for estimating the extent of sea ice. During the Quick Scatterometer (QuikSCAT) mission, SeaWinds data were used to operationally map the sea ice extent. The resulting sea ice maps were used to mask near-surface winds to support SeaWinds' primary mission of measuring near-surface winds over the ocean. This paper describes the operational SeaWinds sea ice extent mapping algorithm, provides validation comparisons, and presents results from the ten-year data product. Starting with enhanced resolution horizontal polarization and vertical polarization backscatter images, the algorithm employs an iterative maximum-likelihood classifier with fixed thresholds to segment sea ice and open ocean pixels. Residual classification errors are reduced through binary image processing techniques and sea ice growth/retreat constraint methods. The algorithm results are compared with sea ice concentrations derived from Special Sensor Microwave/Imager data and with RADARSAT synthetic aperture radar imagery. The results suggest differences in the sensitivities of active and passive products given their channel sets and specific algorithms. Derived sea ice extents over the full decade-long QuikSCAT mission data set are analyzed to show important trends in sea ice extent for the Antarctic and Arctic regions.

Index Terms—Antarctica, Arctic, maximum likelihood (ML) detection, microwave sensors, microwave radiometry, QuikSCAT, radar remote sensing, sea ice, SeaWinds.

I. INTRODUCTION

WIND scatterometers are satellite-borne radars designed to measure near-surface winds over the ocean. They use an indirect method of measuring the wind: The direct measurement is of the normalized radar cross section (σ^o) of the surface from which the wind is estimated using a geophysical model function [1], [2]. The measurements of σ^o have proven useful in a variety of other applications, including the study of polar ice [3]–[9].

The scientific community has a keen interest in monitoring the Earth's cryosphere since these critical regions influence a number of global geophysical processes. The extent of sea

ice has long been considered to be a key component in these processes. For example, the insulating nature of sea ice impedes heat transfer between the relatively warm ocean and cool atmosphere. In addition, sea ice typically reflects a large amount of solar radiation back into space which modifies the levels of energy absorbed by the Earth. Sea ice extent is commonly held to be a sensitive indicator of long-term global climate change [10].

In 1996, National Aeronautics and Space Administration (NASA) launched the Ku-band NASA scatterometer (NSCAT) [1] aboard the Advanced Earth Observing Satellite (ADEOS) platform. However, a solar panel failure terminated the mission before NSCAT completed a full year of observations. In June 1999, NASA launched another Ku-band instrument, SeaWinds, aboard Quick Scatterometer (QuikSCAT) that continued the Ku-band monitoring of ocean surface wind vectors, sea ice, and other important geophysical parameters. The QuikSCAT satellite operated effectively for over ten years before ending its primary science mission in November 2009. A second SeaWinds flew for nine months in 2004 aboard ADEOS-2.

An algorithm to map sea ice from Ku-band NSCAT databased on reconstructed backscatter images was demonstrated in [11]. The algorithm, hereafter known as the Remund/Long-NSCAT (RL-N) algorithm, was validated by comparing the resulting sea ice extent maps with ice concentration imagery generated from Special Sensor Microwave/Imager (SSM/I) data using the NASA Team algorithm. After the end of the NSCAT mission and the launch of QuikSCAT, this ice detection method was modified and adapted for use with SeaWinds. This became the basis of the operational sea ice extent algorithm for QuikSCAT processing over the ten-year mission life.

The purpose of this paper is to describe the QuikSCAT sea ice extent mapping algorithm, the validation work that led to its adoption in the operational processing, and the production of a ten-year independent sea ice extent data product. We provide a limited comparison with sea ice concentration derived from SSM/I data and with RADARSAT synthetic aperture radar (SAR) images. Additional validation is provided in [12]. This paper is organized as follows. Background information about the instrument and the original RL-N ice edge detection algorithm is provided in Section II. Section III describes the SeaWinds data parameters and their levels of sensitivity to the presence of sea ice. The algorithm development is described in Section IV. Section V summarizes the validation results and the application of the algorithm to the full ten-year QuikSCAT data set. Finally, conclusions are presented.

Manuscript received May 9, 2013; revised July 31, 2013; accepted August 20, 2013. Date of publication September 26, 2013; date of current version February 28, 2014.

Q. P. Remund is with the Ball Aerospace and Technologies Corporation, Boulder, CO 80301 USA (e-mail: qremund@ball.com).

D. G. Long is with the Department of Electrical and Computer Engineering, Brigham Young University, Provo, UT 84602 USA (e-mail: long@ee.byu.edu).
Digital Object Identifier 10.1109/TGRS.2013.2281056

II. BACKGROUND

While the RL-N method demonstrated its utility in mapping the spatial distribution of sea ice using NSCAT data, the NSCAT data stream was lost with the failure of the ADEOS satellite in mid-1997. However, in June 1999, another Ku-band scatterometer, SeaWinds on QuikSCAT, was launched. This “quick recovery” mission was initiated to fill the Ku-band data gap left at the end of the NSCAT mission. From 1999 to 2009, this instrument provided a nearly continuous observational data set of ocean, land, and sea ice. SeaWinds is a 13.4-GHz dual-polarization scanning pencil beam scatterometer with two spot beam scans [13]. The outer scan (at 54° incidence) measures vertical polarization (v-pol) σ° while the inner scan (46° incidence) measures horizontal polarization (h-pol) σ° . The resulting swath is 1800 km wide with no nadir gap. Consequently, SeaWinds covered approximately 90% of the Earth’s surface and 100% of the polar regions each day.

SeaWinds has two spatial resolution “modes.” The SeaWinds measurement cells (also called “eggs”) have a nominal resolution of 25–50 km and are collected at various azimuth angles. These cells are further resolved through Doppler filtering, splitting each cell into several elongated “slices” approximately 5–6 km wide by 25–30 km long. Science data products can be made from either egg or slice measurements.

Images of σ° can be generated from SeaWinds measurements using the scatterometer image reconstruction (SIR) algorithm. SIR is an iterative reconstruction method that uses data collected from multiple passes of a satellite to enhance spatial resolution [14]. A tradeoff occurs between temporal resolution, noise amplification, and spatial resolution. For SeaWinds, the SIR algorithm is used to construct v- and h-pol images from egg data on a 4.45-km grid with an effective resolution of approximately 10–12 km. A 4.45-km grid was selected because individual QuikSCAT slices are approximately 5–6 km by 25–30 km, which provides at least one pixel per slice width. For historical reasons, the precise grid used was 4.45 km, to be compatible with image resolutions used for the NSCAT and Advanced Scatterometer data processing. Slice measurements are used to produce enhanced resolution imagery on a 2.225-km grid with an effective resolution of 4–8 km. While the slice images have better spatial resolution, noise levels are inherently higher. For the Arctic and Antarctic regions, both egg and slice images are produced at daily and twice daily intervals by the Scatterometer Climate Record Pathfinder (SCP) (www.scp.byu.edu) project.

The sea ice extent algorithm described in this paper can be applied to polar scatterometer imagery generated on different resolution scales. Due to the computational complexity of the SIR algorithm, for near real time (NRT) operations, slice image products are reconstructed using the average (AVE) algorithm, enabling surface σ° analysis shortly after data acquisition. The AVE technique uses a weighted average of σ° measurements to compute an enhanced resolution estimate for a particular image pixel [15]. The NRT operational processing of polar SeaWinds slice imagery was implemented at the Jet Propulsion Laboratory (JPL) for ocean wind studies and by National Oceanic and Atmospheric Administration and the Brigham Young University SCP for sea ice pack analysis. Image and sea

ice products are available through the JPL Physical Oceanography Distributed Data Active Archive Center (PO.DAAC) and the SCP. While products without resolution enhancement illustrate good performance comparable to historical radiometer products, the added scatterometer capability to enhance image resolution by segmenting the beam-limited footprints through Doppler filtering allows for the examination of finer detail along sea ice edges than is possible using coarser radiometer data products. The SAR image comparisons reported later in this paper illustrate those benefits further.

Since the SeaWinds ice extent mapping algorithm presented in this paper is developed from the RL-N method, it is briefly summarized here. An in-depth description of the RL-N algorithm is given in [11]. The RL-N algorithm uses NSCAT SIR enhanced resolution imagery to generate estimates of the spatial distribution of sea ice. Three basic parameters are used in the RL-N classification. The first is the co-polarization (copol) ratio, γ , of v- and h-pol σ° at 40° incidence. In general, this parameter is low for sea ice and high in open ocean regions [4]. The second metric used in the discrimination is the v-pol incidence angle dependence of σ° , B_v , exhibiting relatively low and high magnitudes for ice and ocean, respectively [4], [16]. The combination of these two parameters along with statistical classification methods shows great utility in identifying sea ice and ocean regions. The third parameter, the σ° estimate error standard deviation, κ , is used to further enhance the edge estimate. Residual errors are minimized using binary image processing techniques. The resulting ice edge correlated well with the SSM/I-derived NASA Team algorithm 30% ice edge during the relatively short-lived NSCAT mission.

Extending the RL-N algorithm to SeaWinds data required several modifications due to the inherent differences between the two instruments. The fan beam configuration of NSCAT allowed for the measurement of σ° at v- and h-pol at multiple incidence angles [1]. In contrast, SeaWinds employs a scanning pencil beam geometry. The distinct fixed incidence angles of the v- and h-pol beams preclude the computation of the two primary RL-N classification parameters, the copol ratio and the incidence angle dependence of σ° . However, modified parameters can be constructed that exhibit significant sensitivity to the presence of sea ice. These are described in the following section. The increased coverage of SeaWinds when compared to NSCAT significantly improves the temporal resolution of the sea ice extent estimates: One day of SeaWinds data can be used to make enhanced resolution images in contrast to NSCAT’s 3–6-day data requirement.

III. SEAWINDS ICE EXTENT MAPPING PARAMETERS

Four primary SeaWinds SIR images are reconstructed for each one-day interval: v-pol σ° at 54° incidence (A_v^{54}), h-pol σ° at 46° incidence (A_h^{46}), and the v- and h-pol σ° estimate error standard deviations (κ_v and κ_h). The pixel value for the standard deviation images is the standard deviation of the difference between the σ° measurements and their forward projection computed from the reconstructed backscatter images and the particular measurement response functions [14]. Sample images are shown in Fig. 1. For later use, we define each

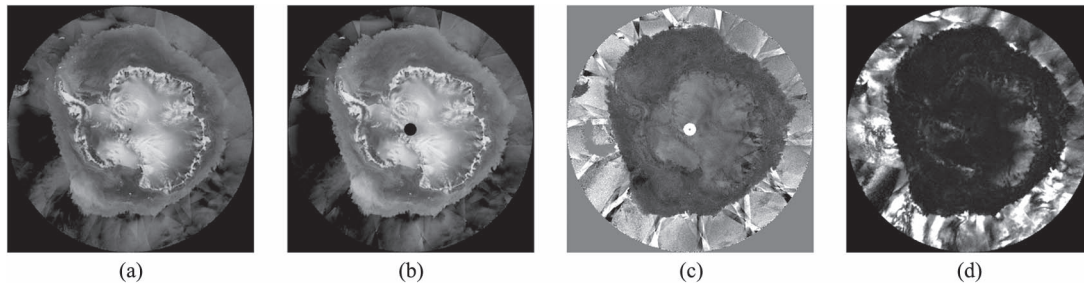


Fig. 1. Sample SeaWinds egg SIR imagery for day 245 of 1999. The images are (a) A_v^{54} , (b) A_h^{46} , (c) γ_{sw} , and (d) κ_v (κ_h is not shown). The original images contain 1940×1940 pixels with a nominal pixel spacing of 4.45 km. In each image frame, lighter shades indicate higher σ^o values in (a) and (b), larger polarization differences in (c), and higher σ^o variability in (d).

of the parameters used in the ice classification and discuss their utility in sea ice detection.

A. Modified Copol Ratio

The first parameter is the modified SeaWinds copol ratio, γ_{sw} , which is defined as the ratio of A_v^{54} and A_h^{46}

$$\gamma_{sw} = A_v^{54} / A_h^{46}. \quad (1)$$

This is equivalent to taking the difference in log space of v- and h-pol σ^o . A sample γ_{sw} image is shown in Fig. 1 to illustrate the sensitivity of this parameter to the presence of sea ice.

The modified SeaWinds copol ratio metric exhibits a combination of two Ku-band backscatter signatures, including the polarization and incidence angle dependences of ocean and sea ice. The utility of the polarization response has been shown in identifying sea ice [4]. In general, sea ice volume scattering produces lower ratios while ocean surface scattering results in higher ratios. The modified SeaWinds copol ratio also contains cross-polarization incidence angle dependence, which is sensitive to surface roughness levels. Incidence angle dependence has been used by a number of researchers to study sea ice [11], [16]–[19]. Sea ice microwave signatures are typically more isotropic in incidence angle than sea water surfaces. Overall, the polarization and incidence angle dependences of σ^o combine such that γ_{sw} is low in the sea ice portions of the image and relatively higher in ocean regions.

B. Horizontal Polarization σ^o

The A_h^{46} image is also useful in discriminating between ocean and sea ice pixels. An example enhanced resolution image of this parameter is shown in Fig. 1. The h-pol measurements over the ocean are typically much lower than their v-pol counterparts while sea ice has similar signatures. Consequently, the h-pol responses of sea ice and open ocean are more easily segmented. Similar to the copol ratio, wind-induced surface roughness can potentially cause ambiguous signatures.

C. Dual-Polarization σ^o Estimate Error Standard Deviation

Two additional parameters are used to complement γ_{sw} and A_h^{46} to increase the ability of the algorithm to separate sea ice and ocean pixels: the v- and h-pol σ^o estimate error standard deviations, κ_v and κ_h . These metrics are reconstructed on the enhanced resolution grid for compatibility with other SIR

products. In general, the κ metric is statistically equivalent to the standard deviation of the difference error between the σ^o measurements touching a pixel and their associated forward projections. Fig. 1 contains a sample κ_v image.

The dual-polarization σ^o estimate error standard deviation parameters are functions of variations in observed σ^o during the imaging interval, primarily due to azimuthal and temporal dependences of surface backscatter. Azimuthal modulation over wind-roughened ocean surfaces increases this metric, while in contrast, sea ice has been shown to have negligible C- and Ku-band azimuthal dependences, generally less than 1 dB [20], [21]. This difference generally increases ocean κ values when compared to sea ice. In addition, temporal variations due to changes in surface scattering mechanisms during the data collection interval cause κ measurements to rise.

IV. MULTIVARIATE SEA ICE EXTENT MAPPING

Through a combination of maximum likelihood (ML) detection and image processing techniques, the sea ice extent can be effectively mapped using γ_{sw} , A_h^{46} , κ_v , and κ_h imagery. This section describes an algorithm designed specifically for SeaWinds Ku-band data. While based on the fundamental methodology of the RL-N method, significant modifications and improvements are presented. The method can be broken down into five major steps beginning with the parameter images described previously:

- 1) data fusion and histogram generation;
- 2) linear discrimination;
- 3) iterative ML discrimination;
- 4) residual error reduction;
- 5) sea ice growth/retreat constraint filtering.

Each of these steps is described in the following sections.

A. Data Fusion and Histogram Generation

Individually, each of the four classification parameters contains valuable information about the presence of sea ice. Taken together, a more accurate classification is possible. These data reside in a 4-D hyperspace of measurement vectors

$$\vec{x} = [\gamma_{sw} A_h^{46} \kappa_v \kappa_h]^T. \quad (2)$$

The data fusion portion of the algorithm ensures that data are weighted to maximize classification accuracy. The first step consists of data standardization. Each of the three different data

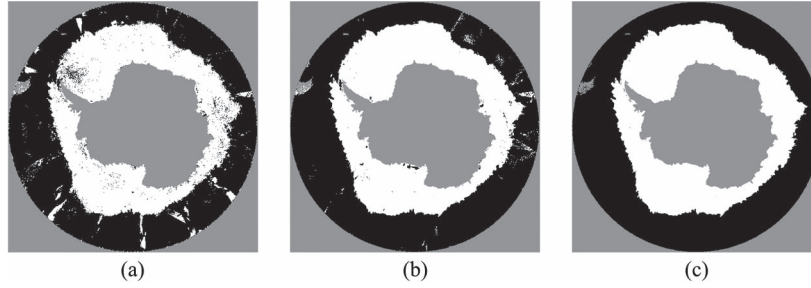


Fig. 2. Sample binary Antarctic ice maps for day 245 of 1999 at various stages in the algorithm: (a) Initial linear discrimination estimate, (b) iterative ML estimate, and (c) classification error filtered estimate.

types (γ , A_h , and κ) is normalized such that each type has a mean of zero and a variance of one. This transforms the hyperspace so that each parameter type is initially given equal weight. An additional weighting factor is applied to account for the fact that each parameter contains varying levels of sea ice detection information. An empirical analysis revealed that a weighting value of four applied to γ_{sw} with unity weighting for the other parameters produces good sea ice detection performance.

Once the data are prepared through standardization and vector weighting, the distribution of observation vectors is examined through histogram analysis. The 4-D histogram of the data space is generated, revealing a bimodal sea ice/ocean joint distribution. The sea ice distribution has a typically tighter covariance structure than the ocean distribution. Due to the temporal variability of both sea ice and ocean distributions, a fixed boundary cannot be used to segment the two clusters throughout the year. Rather, an effective algorithm must have the ability to adapt to current conditions to provide an optimal estimate of sea ice extent. The following sections detail the iterative portion of the algorithm to achieve automated adaptability in cluster discrimination.

B. Linear Discrimination

The first classification is achieved through linear discrimination using a hyperplane boundary to segment the two component distributions. To identify the initial boundary, the distribution modes are first found through an automated 4-D histogram search algorithm. The saddle point of the histogram values along the transect connecting the two modes is chosen for the location to place the transect-orthogonal hyperplane discrimination boundary.

Fig. 2 shows three binary ice masks resulting from various stages of the algorithm for a sample image set in Antarctica. Fig. 2(a) depicts the ice extent estimate after the linear discrimination. While the ice edge can be readily observed, errors still exist, indicating that further processing is required to improve the ice extent estimate.

C. Iterative ML Discrimination

While the linear discrimination method produces a reasonable initial estimate of the ice edge, higher order classifiers can improve the quality of the final sea ice map. For the SeaWinds data, we use an ML classification technique adopted from a study to identify sea ice types in Antarctica [6]. An ML clas-

sifier is derived assuming that the two component distributions are Gaussian in the hyperspace. The Gaussian assumption was adopted to facilitate the real-time implementation of the algorithm and allows for the use of standard, but powerful, statistical estimation techniques. Other investigators, including Anderson and Long [22], used derived histograms to approximate the distributions. This provided some improvement; however, the baseline algorithm used for NRT processing maintains the use of the Gaussian approximation since it can be easily parameterized by means and variances.

Under the multivariate Gaussian assumption, an ML detection algorithm reduces to the minimization of an “ML distance metric”

$$C_{ML} = \underset{c}{\operatorname{argmin}} [\log|K_c| + (\vec{y} - \vec{\mu}_c)^T K_c^{-1} (\vec{y} - \vec{\mu}_c)] \quad (3)$$

where \vec{y} is the standardized and weighted data vector, $\vec{\mu}_c$ is the mean vector for surface type C , and K_c is the covariance matrix for that surface type. The ML method results in a quadratic boundary which accounts for the differences in component distribution variances and covariances.

Using estimates of the mean vectors and covariance matrices of the two clusters computed from the initial linear discrimination, the ML classification is employed. After the first implementation of the ML method, the statistics are updated, and the ML classification is used once more. Within two iterations, the algorithm converges to an improved estimate of the polar sea ice extent. A sample of the resulting binary ice masks is given in Fig. 2(b). Compared with the linear discrimination results [see Fig. 2(a)], significant improvements have been made, although some residual errors are still present in the images.

D. Residual Error Reduction

The ML estimate of the sea ice extent can still contain some misclassifications due to high persistent winds over a region during the imaging period which can result in ambiguous signatures that confuse the algorithm. Isolated regions of misclassified pixels can be eliminated through the use of the binary image processing technique of region growing. As described in [11], the region growing technique is used to identify and remove small patches of ocean misclassified as sea ice and vice versa. Unfortunately, the algorithm filters out polynyas as well. Since the objective of this study is to identify the total sea ice extent, ice-free polynya regions are included in the extent estimate. However, the processing can be adjusted

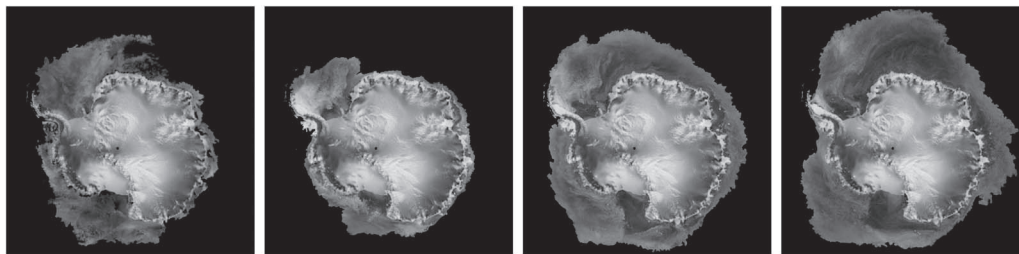


Fig. 3. Sample ice-masked SeaWinds v-pol images illustrating the seasonal evolution of Antarctic sea ice extent. The images are (from left to right) days 1, 92, 183, and 274 for the year 2008.

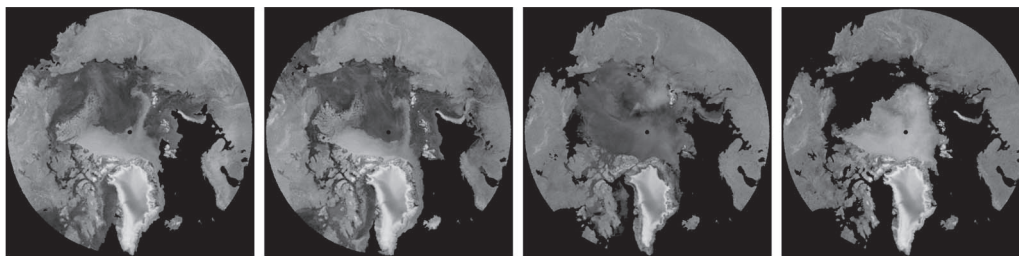


Fig. 4. Sample ice-masked SeaWinds v-pol images illustrating the seasonal evolution of Arctic sea ice extent. The images are (from left to right) days 1, 92, 183, and 274 for the year 2008.

to retain polynyas along with the infrequent misclassifications within the ice pack by skipping the inverse region growing step. An example of the effect of region growing on the ice extent estimate is shown in Fig. 2(c).

E. Sea Ice Growth/Retreat Constraint Filtering

While the algorithm steps described earlier work for the majority of observed data, rare cases of additional errors are observed in the form of infrequent misclassified “extrusions” or “indentation” along the ice edge. Using image dilation and erosion techniques [23], [24], the previous day’s ice extent map is combined with typical sea ice growth and retreat rates to constrain allowable ice motion. A binary difference image between adjacent days’ images is used to detect areas where the ice grew or retreated faster than a user-defined maximum edge change. For this study, a 200-km maximum edge motion per day threshold, for both ice growth and retreat, produces good results in eliminating erroneous spurious ice extrusions or indentations.

V. RESULTS

As noted previously, the sea ice extent algorithm was developed early in the QuikSCAT mission and applied daily to produce operational Antarctic and Arctic ice extent imagery of the full 1999–2009 QuikSCAT SeaWinds data set. Enhanced resolution imagery was produced on one-day intervals, resulting in a large time series of ice-masked imagery that can be used for a number of applications. Examples are the removal of sea ice regions in scatterometer wind processing and ice edge evolution studies. In this section, the QuikSCAT-generated ice extent maps are validated and analyzed. For validation, comparisons are made with ice edges produced by the NASA Team algorithm applied to SSM/I data in both polar regions and RADARSAT SAR imagery in the Arctic. The evolution of the

total sea ice extent is also studied during the SeaWinds mission and compared with the corresponding SSM/I-derived trends.

A. Ice-Masked Polar Image Sequences

Fig. 3 shows four sample ice-masked SeaWinds A_v^{54} images of Antarctica. The image series demonstrates the dynamic nature of Antarctic sea ice throughout the seasonal cycle. The first image shows the state of the sea ice pack at the beginning of the 2008 calendar year representing a phase of rapid sea ice retreat during austral summer. The following image, day 92, shows the distribution of sea ice after the summer minimum was reached and ice advance had ensued. By day 183, the ice pack expanded substantially, reaching nearly its maximum extent at day 274. The daily time series of images over the QuikSCAT mission is useful for studying the seasonal variation of the ice pack and its response to atmospheric forcing.

Within the ice pack, a wide spectrum of σ^o values is observed. The various levels of backscatter are related to sea ice properties such as surface roughness, snow cover, dielectric loss, and volume scattering due to inhomogeneities. In general, older ice types appear very bright in the imagery due to increased volume scattering as water and brine content drain from the ice. Very rough ice types also exhibit high backscatter. Young smooth ice forms have much lower σ^o values. Consequently, the evolution of surface features can be monitored to better understand polar sea ice dynamics. For example, from day 92 to day 183, brighter relatively old ice moves away from the Ronne and Ross Ice Shelves due to ocean currents and prevailing surface winds. Younger forms of ice fill in the gap shown by the low backscatter region along the shelf.

Fig. 4 illustrates a similar image series for the Arctic region. Again, the dynamic nature of sea ice extent is observed. The first image frame, representing the first day of 2008, shows the Arctic sea ice distribution as the ice pack expands outward.

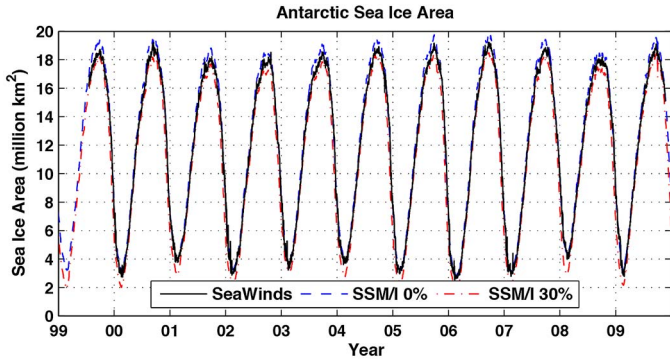


Fig. 5. Antarctic daily total sea ice area during the QuikSCAT operational mission. The QuikSCAT and SSM/I 0% and 30% ice extents are shown.

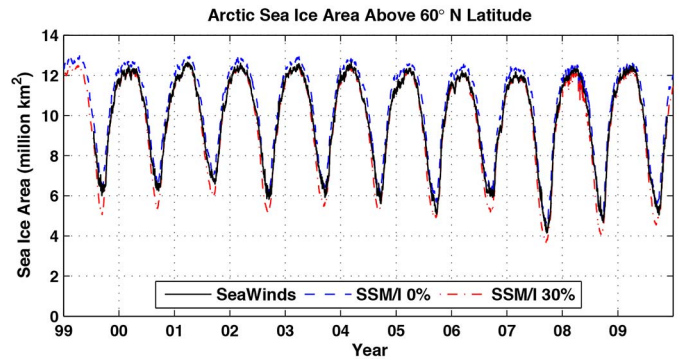


Fig. 6. Arctic daily total sea ice area above 60° N latitude during the QuikSCAT operational mission. The QuikSCAT and SSM/I 0% and 30% ice extents are shown.

Regions of high-backscatter multiyear ice are clearly evident in contrast to younger lower backscatter ice. The image frame representing day 92 shows the ice pack near its maximum extent. Note that the map projection used for these images stops at 60° north latitude, so the full ice extent is not observed in some areas. At day 183, the sea ice pack has retreated substantially. Finally, day 274 illustrates the ice extent near the minimal point during the year. During this period, the high-backscatter multiyear sea ice constitutes a large majority of the ice pack. The image sequence shows the relative motions of old and young sea ice throughout the season.

B. SSM/I NASA Team Algorithm Comparisons

The total sea ice extent area can be obtained from the ice-masked imagery. This parameter is computed by summing the areas of all ice flagged pixels in the QuikSCAT or SSM/I images. To validate the QuikSCAT sea ice algorithm, the SeaWinds ice extent images are compared with SSM/I-derived sea ice concentration imagery produced by the NASA Team algorithm (provided by the National Snow and Ice Data Center). The NASA Team method uses multifrequency dual-polarization data from the SSM/I microwave radiometer to produce estimates of sea ice concentration on a 25-km grid [25]–[27]. Both the SSM/I NASA Team and QuikSCAT SeaWinds images are presented using similar polar stereographic projections. The QuikSCAT egg images are produced on a higher resolution grid with pixel spacing of 4.45 km. Daily ice concentration images are compared with QuikSCAT data by interpolating the SSM/I ice concentration imagery to the same pixel grid. These are then thresholded at various concentration levels to obtain multiple ice edges for comparison.

The QuikSCAT Antarctic total ice area results for the entire 1999–2009 operational mission are shown in Fig. 5. The SSM/I-derived 0% and 30% ice concentration extent values are shown for comparison. The plots illustrate the overall variability in seasonal and annual ice extents over the course of the ten-year period. We find that the QuikSCAT ice extents fall within the 0%–30% SSM/I ice concentration range. A more extensive evaluation of the QuikSCAT- and SSM/I-derived edges for the Antarctic is given in [12].

Arctic results are shown in Fig. 6. Note that, in this paper, the Arctic ice extent is only mapped above 60° north latitude. Consequently, the maxima shown in the figure are effectively

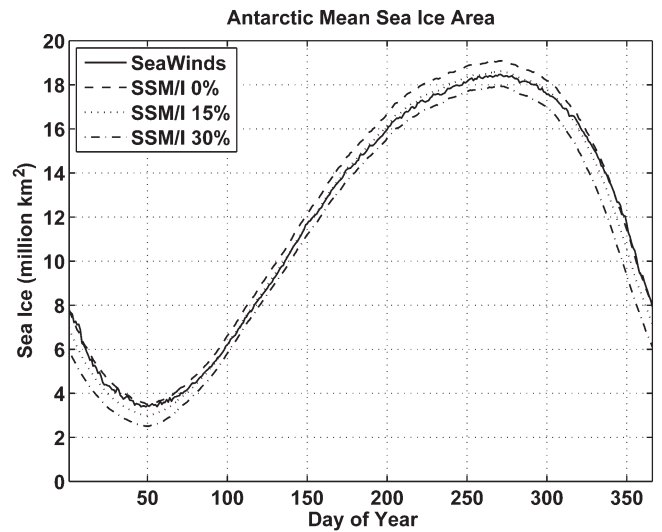


Fig. 7. Mean daily Antarctic total sea ice area during the QuikSCAT operational mission. QuikSCAT and SSM/I 0%, 15%, and 30% ice extents are shown for comparison.

truncated and do not show the full maximum values that include sea ice at lower latitudes at the peak of Arctic winter. Similar to the Southern Hemisphere, we observe that the QuikSCAT ice extent falls within the SSM/I-derived 0%–30% ice concentration range. A more extensive evaluation of the QuikSCAT- and SSM/I-derived edges for the Arctic is given in [12].

A seasonal comparison is shown in Fig. 7 for the Antarctic and Fig. 8 for the Arctic, which include plots of the mean ice extent areas for each calendar day. For each day of the year, the QuikSCAT ice extents were averaged over all years during the QuikSCAT mission period. The corresponding 0%, 15%, and 30% SSM/I ice concentration extents are shown as well. For the Antarctic results, we observe that the QuikSCAT extent correlates very well with the SSM/I 0% extent during the ice ablation phase and with the 15% extent during ice pack growth. The Arctic results also show reasonably good correlation with the 15% edge during ice advance, but the QuikSCAT extent during the melt phase varies more widely between 0% and 30%.

To further illustrate the edge comparisons, Fig. 9 shows a QuikSCAT A_h^{46} image of the Weddell Sea quadrant of Antarctica for day 245 of 1999. Several ice edge contours are superimposed on the figure. The white contour is the QuikSCAT-derived edge while the NASA Team 5% and 30%

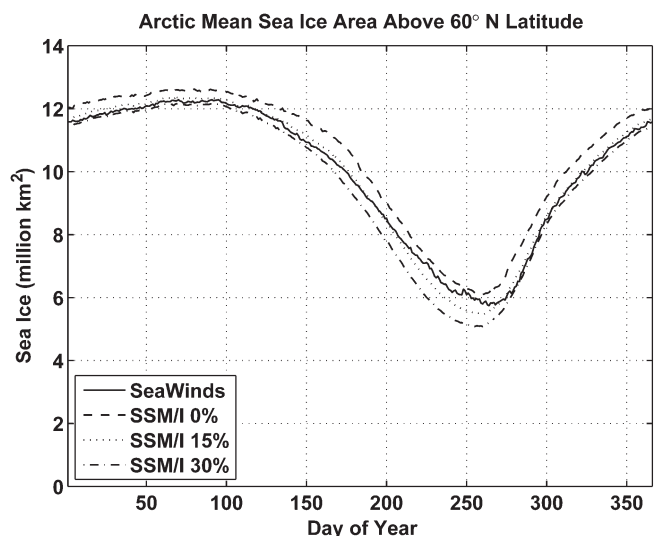


Fig. 8. Mean daily Arctic total sea ice area above 60° N latitude during the QuikSCAT operational mission. QuikSCAT and SSM/I 0%, 15%, and 30% ice extents are shown for comparison.

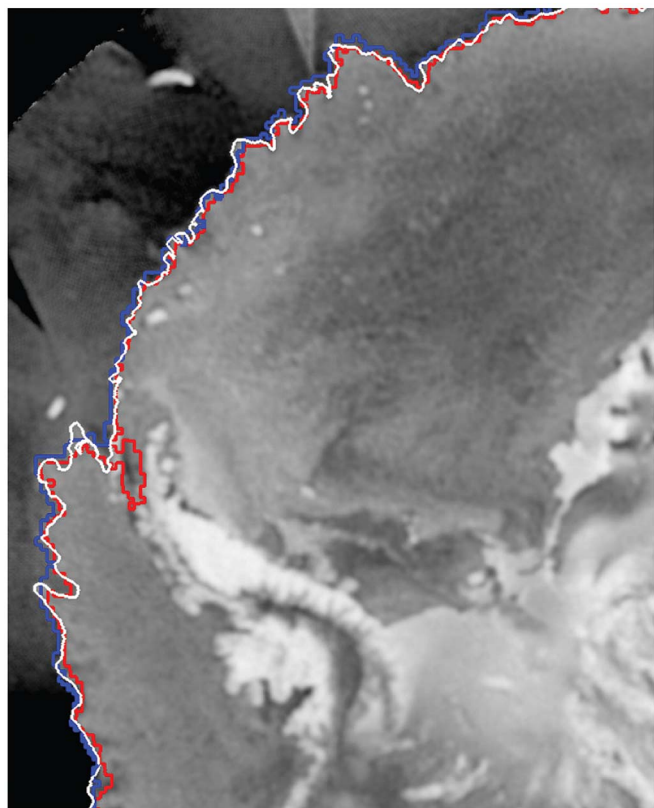


Fig. 9. Sea ice edge comparisons in the Weddell Sea quadrant of Antarctica for day 245 of 1999. The SSM/I NASA Team 5% and 30% ice edges are plotted in blue and red, respectively. The white contour is the QuikSCAT edge.

concentration edges are shown in blue and red, respectively. The figure shows that the QuikSCAT edge generally tracks between the 5% and 30% contours. A similar image is shown in Fig. 10 for day 5 of 2000. Again, all three edges are plotted. While, in this case, the closest correlation is observed between the QuikSCAT and 5% contours, significant discrepancies exist. In particular, the QuikSCAT edge is further north than low NASA Team concentrations. Similar trends in compar-

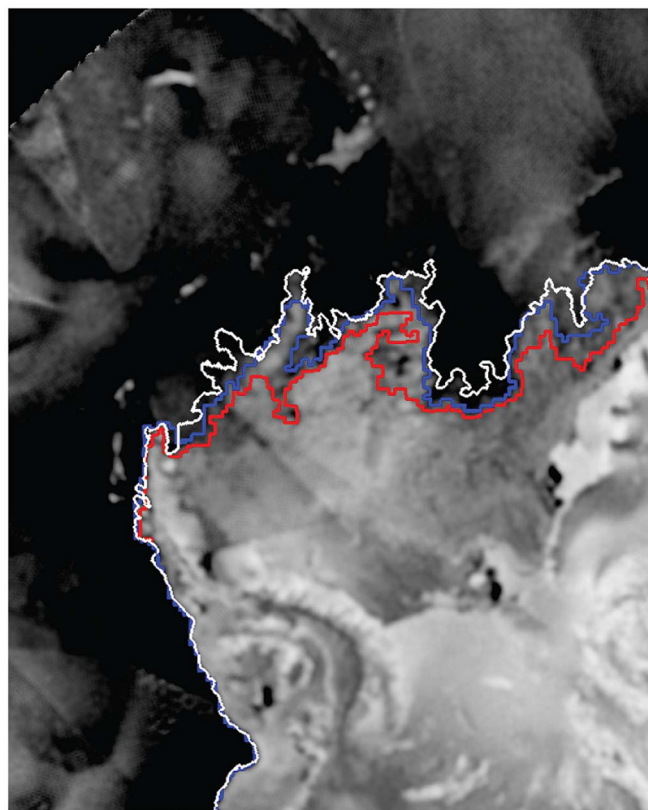


Fig. 10. Sea ice edge comparisons in the Weddell Sea quadrant of Antarctica for day 5 of 2000. The SSM/I NASA Team 5% and 30% ice edges are plotted in blue and red, respectively. The white contour is the QuikSCAT edge.

ing Geodetic Satellite radar altimeter ice edges with NASA Team ice concentrations during ice ablation have been previously observed, which found that the radar-derived extent was consistently larger than the SSM/I-derived product [28]. Taken together, these results suggest differences in the sensitivities of selected frequencies, polarizations, algorithm methodologies, and active versus passive microwave measurements to sea ice concentrations as the ice edge recedes. A detailed analysis of this difference is beyond the scope of this paper.

C. Comparison With Arctic RADARSAT SAR Imagery

With high spatial resolution but limited coverage, SAR imagery can be beneficial for ice edge validation in small localized regions. Although SAR imagery of sea ice edges is less common in the Antarctic, an abundance of image frames is available in the Arctic. For this study, a number of RADARSAT h-pol C-band SAR image frames were obtained from the National Ice Center. The images cover sea ice edge regions near Greenland during February 2000. Several sample RADARSAT images are shown in Fig. 11. Superimposed on each frame are the SeaWinds and the NASA Team 5% and 30% ice edge estimates. In general, the observed RADARSAT and SeaWinds edges are highly correlated, matching each other within approximately 10 km. The NASA Team algorithm edge contours also provide good estimates of the sea ice edge although at a lower resolution.

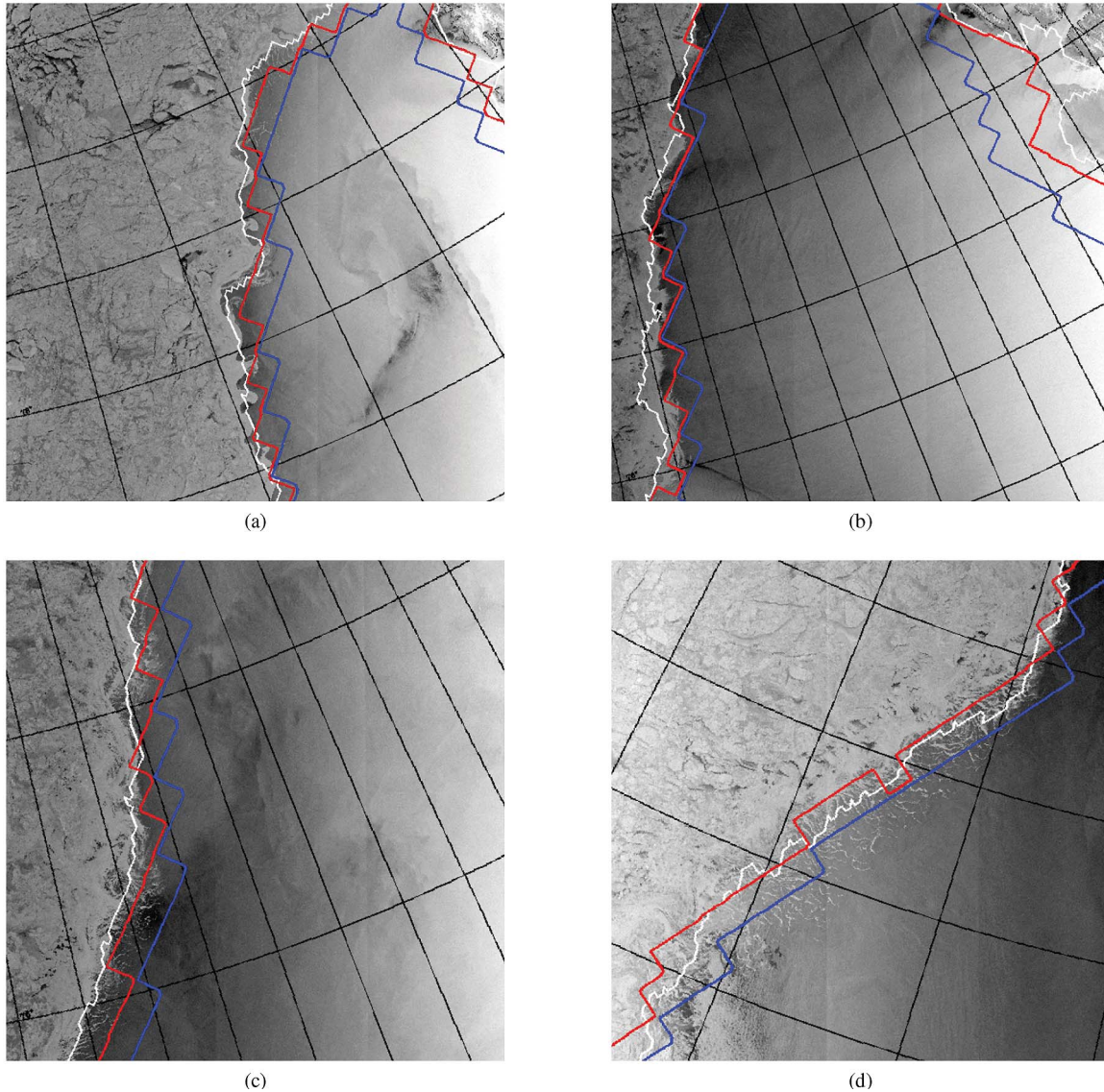


Fig. 11. RADARSAT images with (white) QuikSCAT and SSM/I NASA Team (blue) 5% and (red) 30% edge estimates. The image acquisition days are (from top left to bottom right) days 37, 38, 48, and 51 of 2000. (RADARSAT-1 data 2001, Canadian Space Agency).

We note that, while the RADARSAT images are essentially instantaneous “snapshots” made as the satellite passed over the region, the SeaWinds and NASA Team edges were created using a full day of microwave data. Consequently, the SeaWinds and SSM/I edges represent averages over the entire day. We expect some differences to be evident since sea ice edges can be very dynamic, moving several kilometers in a single day.

Fig. 11 also illustrates the behavior of the algorithm under different edge conditions. For example, the algorithm’s performance varies when the sea ice edge is sharp rather than diffuse. When the sea ice edge is clearly defined, the technique estimates the location of the edge relatively well. As the edge becomes more diffuse, the QuikSCAT edge does not identify the lowest concentrations as sea ice.

D. Minimum Sea Ice Extent Evolution

A key metric monitored by climate scientists is the annual minimum sea ice area in the northern and southern polar re-

gions. Figs. 5 and 6 show the evolution of the minimum sea ice areas for the Antarctic and Arctic, respectively, as measured by QuikSCAT. The corresponding sea ice extent images are shown in Figs. 12 and 13. For the Antarctic, the lowest value observed during the QuikSCAT mission was in 2006 at 2.54 million km^2 , and the highest value was in 2008 at 3.98 million km^2 , with a mean of 3.17 million km^2 and a standard deviation of 0.51 million km^2 . The Arctic values included a low value in 2007 at 4.15 million km^2 , a high value of 6.59 million km^2 during 2001, a mean of 5.5 million km^2 , and a standard deviation of 0.73 million km^2 .

VI. CONCLUSION

Previous studies have shown that Ku-band scatterometer data are capable of effectively discriminating between open ocean and sea ice. This paper describes an algorithm which was developed for the SeaWinds scatterometer on QuikSCAT and which was used for its operational processing [2]. The

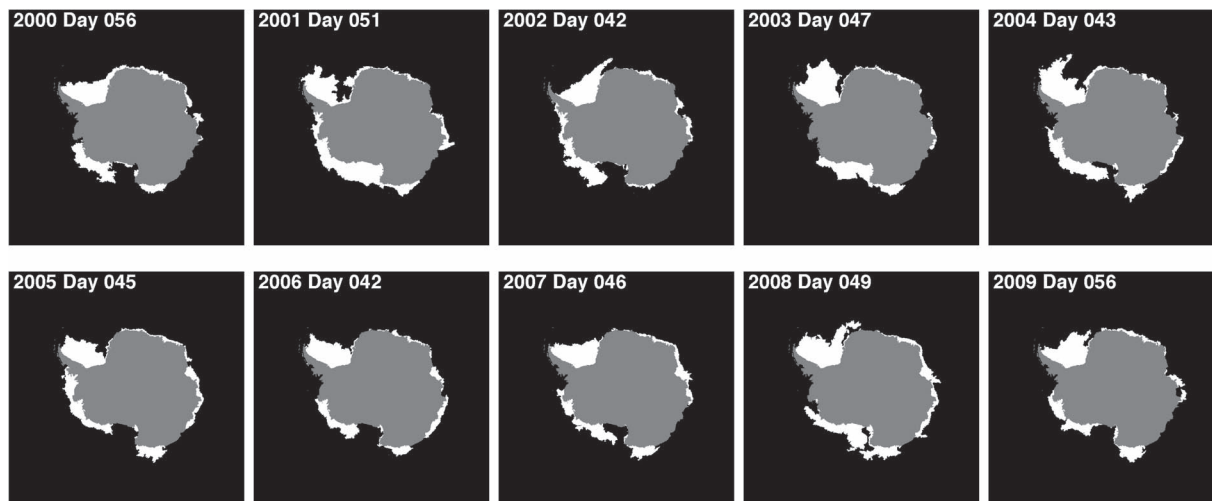


Fig. 12. Ice mask images illustrating the annual minimum Antarctic sea ice extent during the QuikSCAT operational mission. For each year, the daily ice mask exhibiting the lowest total sea ice area is shown.

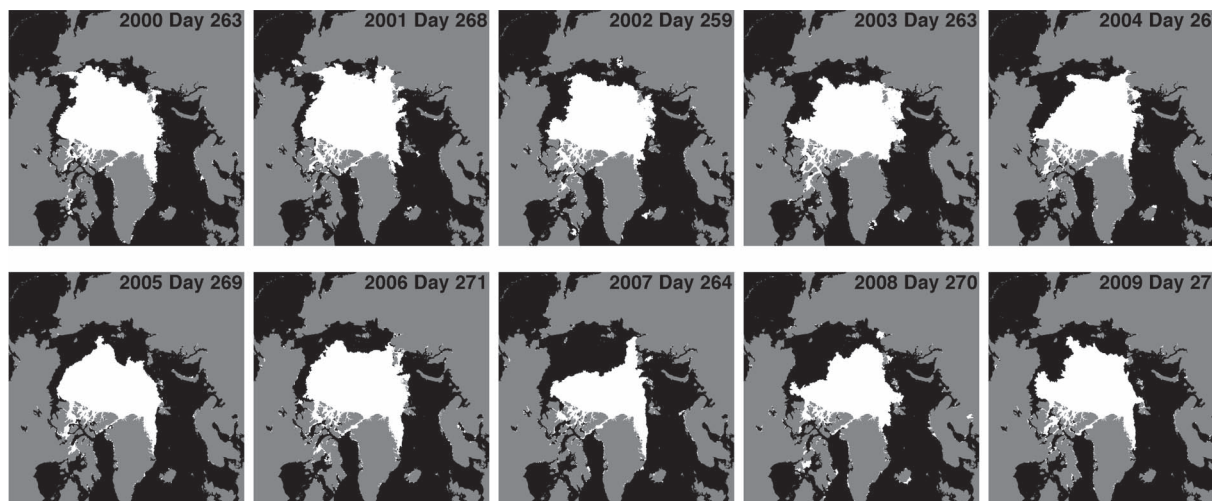


Fig. 13. Ice mask images illustrating the annual minimum Arctic sea ice extent during the QuikSCAT operational mission. For each year, the daily ice mask exhibiting the lowest total sea ice area is shown.

sea ice mapping algorithm was used operationally over the course of the ten-year mission. The technique is fully automated and adapts to temporally changing surface signatures. The resulting ice edges correlate well with the SSM/I-derived NASA Team algorithm 15%–30% ice concentration contours during ice advance and with the SSM/I-derived NASA Team algorithm 0%–30% ice concentration contours during sea ice retreat. The seasonally dependent correlations suggest differences in the sensitivities of the products to sea ice extent due to active/passive sensing, channel frequencies, channel polarizations, and algorithm methodologies. The method works effectively for the Antarctic and Arctic regimes as demonstrated by comparisons with SSM/I-derived ice concentration maps and high-resolution RADARSAT SAR imagery.

Four microwave parameters are used in the classification: the modified polarization ratio, the SeaWinds h-pol σ^o , and the dual-polarization σ^o estimate error standard deviations. The combination of these parameters is proven effective in identifying sea ice versus ocean regions in enhanced resolution

polar imagery. This study shows that the SeaWinds κ images contain more information about sea ice spatial distribution than their NSCAT counterparts. This is primarily due to the one-day SeaWinds imaging interval which reduces the temporal dependence of the metric and effectively increases sensitivity to azimuthal variations.

The development of the described technique resulted in the ability to generate enhanced resolution sea ice extent maps on one-day intervals. The full ten-year QuikSCAT data set is composed of over 3700 daily ice-masked images of the Antarctic and Arctic sea ice showing the short- and long-term dynamics of these regions. These areas are available from the SCP (www.scp.byu.edu) or the JPL PO.DAAC (podaac.jpl.nasa.gov). The sea ice products have been applied in a variety of studies, including ocean wind processing, sea ice extent evolution, and global climate and weather studies. Since the original development of this algorithm, a number of algorithm improvements have been proposed [8], [22] for processing future scatterometer data sets.

ACKNOWLEDGMENT

The SeaWinds data were obtained from the Physical Oceanography Distributed Data Active Archive Center at the Jet Propulsion Laboratory, Pasadena, California. The NASA Team sea ice concentration imagery was obtained courtesy of the National Snow and Ice Data Center, Boulder, Colorado. The RADARSAT synthetic-aperture-radar images were provided by the National Ice Center and are copyrighted by the Canadian Space Agency. The authors would like to thank K. Stuart who assisted in the data processing for the study and the editor and reviewers whose insightful comments offered significant improvements to this paper.

REFERENCES

- [1] F. Naderi, M. Freilich, and D. Long, "Spaceborne radar measurement of wind velocity over the ocean—An overview of the NSCAT scatterometer system," in *Proc. IEEE*, Jun. 1991, vol. 79, no. 6, pp. 850–866.
- [2] P. Chang, Z. Jelenak, J. Sienkiewicz, R. Knabb, M. Brennan, D. Long, and M. Freeberg, "Operational use and impact of satellite remotely sensed ocean surface vector winds in the marine warning and forecasting environment," *Oceanography*, vol. 22, no. 2, pp. 194–207, 2009.
- [3] D. Long and M. Drinkwater, "Greenland ice-sheet surface properties observed by the Seasat-A scatterometer at enhanced resolution," *J. Glaciol.*, vol. 40, no. 135, pp. 213–230, 1994.
- [4] S. Yueh, R. Kwok, S. Lou, and W. Tsai, "Sea ice identification using dual-polarized ku-band scatterometer data," *IEEE Trans. Geosci. Remote Sens.*, vol. 35, no. 3, pp. 560–569, May 1997.
- [5] D. Long and M. Drinkwater, "Cryosphere applications of NSCAT data," *IEEE Trans. Geosci. Remote Sens.*, vol. 37, no. 3, pp. 1671–1684, May 1999.
- [6] Q. Remund and D. Long, "An iterative approach to multisensor sea ice classification," *IEEE Trans. Geosci. Remote Sens.*, vol. 38, no. 4, pp. 1843–1856, Jul. 2000.
- [7] S. Howell, C. Derksen, and A. Tivy, "Development of a water clear of sea ice detection algorithm from enhanced SeaWinds/QuikSCAT and AMSR-E measurements," *Remote Sens. Environ.*, vol. 114, no. 11, pp. 2594–2609, 2010.
- [8] M. Rivas and A. Stoffelen, "New Bayesian algorithm for sea ice detection with QuikSCAT," *IEEE Trans. Geosci. Remote Sens.*, vol. 49, no. 6, pp. 1894–1901, Jun. 2011.
- [9] A. Swan and D. Long, "Multi-year Arctic sea ice classification using QuikSCAT," *IEEE Trans. Geosci. Remote Sens.*, vol. 50, no. 9, pp. 3317–3326, Sep. 2012.
- [10] W. Budd, "Antarctic sea ice variations from satellite sensing in relation to climate," *J. Glaciol.*, vol. 15, no. 73, pp. 417–426, 1975.
- [11] Q. Remund and D. Long, "Sea-ice extent mapping using ku-band scatterometer data," *J. Geophys. Res.*, vol. 104, no. C5, pp. 11515–11527, May 1999.
- [12] W. Meier and J. Stroeve, "Comparison of sea ice extent and ice edge location estimates from passive microwave and enhanced resolution scatterometer data," *Ann. Glaciol.*, vol. 48, no. 1, pp. 65–70, Jun. 2008.
- [13] M. Spencer, C. Wu, and D. Long, "Tradeoffs in the design of a spaceborne scanning pencil beam scatterometer: Applications to SeaWinds," *IEEE Trans. Geosci. Remote Sens.*, vol. 35, no. 1, pp. 115–126, Jan. 1997.
- [14] D. Early and D. Long, "Image reconstruction and enhanced resolution imaging from irregular samples," *IEEE Trans. Geosci. Remote Sens.*, vol. 39, no. 2, pp. 291–302, Feb. 2001.
- [15] D. Long, P. Hardin, and P. Whiting, "Resolution enhancement of spaceborne scatterometer data," *IEEE Trans. Geosci. Remote Sens.*, vol. 31, no. 3, pp. 700–715, May 1993.
- [16] J. Rouse, "Arctic ice type identification by radar," *Proc. IEEE*, vol. 57, no. 4, pp. 605–611, Apr. 1969.
- [17] M. Drinkwater, *Active Microwave Remote Sensing Observations of Weddell Sea Ice*. Washington DC, USA: AGU, 1998.
- [18] F. Gohin and A. Cavanie, "A first try at identification of sea ice using the three beam scatterometer of ERS-1," *Int. J. Remote Sens.*, vol. 15, no. 6, pp. 1221–1228, 1994.
- [19] F. Gohin, "Some active and passive microwave signatures of Antarctic sea ice from mid-winter to spring 1991," *Int. J. Remote Sens.*, vol. 16, no. 11, pp. 2031–2054, Jul. 1995.
- [20] D. Early and D. Long, "Azimuthal modulation of c-band scatterometer σ^0 over southern ocean sea ice," *IEEE Trans. Geosci. Remote Sens.*, vol. 35, no. 5, pp. 1201–1209, Sep. 1997.
- [21] Q. Remund, D. Early, and D. Long, "Azimuthal modulation of Ku-band scatterometer σ^0 over the Antarctic," mERS, Provo, UT, USA, Tech. Rep. 97-02, 1997.
- [22] H. Anderson and D. Long, "Sea ice mapping method for SeaWinds," *IEEE Trans. Geosci. Remote Sens.*, vol. 43, no. 3, pp. 647–657, Mar. 2005.
- [23] J. Rush, *The Image Processing Handbook*, 2nd ed. Boca Raton, FL, USA: CRC Press, 1995.
- [24] W. Pratt, *Digital Image Processing*, 2nd ed. New York, NY, USA: Wiley, 1991.
- [25] D. Cavalieri, P. Gloersen, and W. Campbell, "Determination of sea ice parameters with the Nimbus-7 SMMR," *J. Geophys. Res.*, vol. 89, no. D4, pp. 5355–5369, Jun. 1984.
- [26] D. Cavalieri, J. Crawford, M. Drinkwater, D. Eppler, L. Farmer, R. Jentz, and E. Wackerman, "Aircraft active and passive microwave validation of sea ice concentration from the defense meteorological satellite program special sensor microwave imager," *J. Geophys. Res.*, vol. 96, no. C12, pp. 21989–22008, Dec. 1991.
- [27] D. Cavalieri, C. Parkinson, P. Gloerson, and H. Zwally, *Sea Ice Concentrations from Nimbus-7 SSMR and DMSP SSM/I-SSMIS Passive Microwave Data*. Boulder, CO, USA: NASA DAAC at the National Snow and Ice Data Center, 1996, updated yearly.
- [28] F. Fetterer, M. Drinkwater, K. Jezek, S. Laxon, R. Onstott, and L. Ulander, *Sea Ice Altimetry*. Washington DC, USA: AGU, 1992, pp. 111–135.

Quinn P. Remund (S'98–M'00) received the Ph.D. degree in electrical and computer engineering from Brigham Young University, Provo, UT, USA, in 2000, where he studied microwave remote sensing with an emphasis in multisensor remote sensing of the cryosphere.

He is currently with the Ball Aerospace and Technologies Corporation, Boulder, CO, USA, where he works on the development of spaceborne UV, visible, infrared, and microwave remote sensing instruments.



David G. Long (S'80–SM'98–F'08) received the Ph.D. degree in electrical engineering from the University of Southern California, Los Angeles, CA, USA, in 1989.

From 1983 to 1990, he worked for NASA's Jet Propulsion Laboratory (JPL) where he developed advanced radar remote sensing systems. While at JPL, he was the Project Engineer on the NASA Scatterometer project which flew from 1996 to 1997. He also managed the Scanning Scatterometer project, the precursor to SeaWinds which was launched in

1999 on QuikSCAT and 2002 on ADEOS-II. He is currently a Professor with the Department of Electrical and Computer Engineering, Brigham Young University, Provo, UT, USA, where he teaches upper division and graduate courses in communications, microwave remote sensing, radar, and signal processing and is the Director of the Brigham Young University Center for Remote Sensing. He is the principle investigator on several NASA-sponsored research projects in remote sensing. He has over 400 publications in various areas, including signal processing, radar scatterometry, and synthetic aperture radar. His research interests include microwave remote sensing, radar theory, space-based sensing, estimation theory, signal processing, and mesoscale atmospheric dynamics.

Dr. Long has received the NASA Certificate of Recognition several times and is an Associate Editor for the IEEE GEOSCIENCE AND REMOTE SENSING LETTERS.